∂A Global Surface Ocean fCO$_2$ Climatology Based on a Feed-Forward Neural Network

J. ZENG AND Y. NOJIRI

Centre for Global Environmental Research, National Institute for Environmental Studies, Tsukuba, Japan

P. LANDSCHÜTZER

School of Environmental Sciences, University of East Anglia, Norwich, United Kingdom

M. TELSZEWSKI

*International Ocean Carbon Coordination Project, Institute of Oceanology,
Polish Academy of Sciences, Sopot, Poland*

S. NAKAOKA

Centre for Global Environmental Research, National Institute for Environmental Studies, Tsukuba, Japan

(Manuscript received 19 June 2013, in final form 21 February 2014)

ABSTRACT

A feed-forward neural network is used to create a monthly climatology of the sea surface fugacity of CO$_2$ (fCO$_2$) on a $1° \times 1°$ spatial resolution. Using 127 880 data points from 1990 to 2011 in the track-gridded database of the Surface Ocean CO$_2$ Atlas version 2.0 (Bakker et al.), the model yields a global mean fCO$_2$ increase rate of 1.50 μatm yr^{-1}. The rate was used to normalize multiple years' fCO$_2$ observations to the reference year of 2000. A total of 73 265 data points from the normalized data were used to model the global fCO$_2$ climatology. The model simulates monthly fCO$_2$ distributions that agree well with observations and yields an anthropogenic CO$_2$ update of -1.9 to -2.3 PgC yr^{-1}. The range reflects the uncertainty related to using different wind products for the flux calculation. This estimate is in good agreement with the recently derived best estimate by Wanninkhof et al. The model product benefits from a finer spatial resolution compared to the product of Lamont–Doherty Earth Observatory (Takahashi et al.), which is currently the most frequently used product. It therefore has the potential to improve estimates of the global ocean CO$_2$ uptake. The method's benefits include but are not limited to the following: (i) a fixed structure is not required to model fCO$_2$ as a nonlinear function of biogeochemical variables, (ii) only one neural network configuration is sufficient to model global fCO$_2$ in all seasons, and (iii) the model can be extended to produce global fCO$_2$ maps at a higher resolution in time and space as long as the required data for input variables are available.

1. Introduction

It has been estimated that the global ocean absorbs nearly half the total emissions of anthropogenic carbon dioxide (CO$_2$) from the atmosphere (Sabine et al. 2004; Jacobson et al. 2007; Gruber et al. 2009; Takahashi et al. 2009). The surface ocean shows much more CO$_2$ variability spatially than the atmosphere, as is shown in Komhyr et al. (1985) and Takahashi et al. (2009); hence, it is import to accurately quantify the oceanic CO$_2$ distribution in order to improve our understanding of the ocean carbon sink. Meanwhile, in spite of many years' efforts by researchers to measure the sea surface CO$_2$ partial pressure (e.g., Feely et al. 1987; Inoue et al. 1995; Cooper et al. 1998; Bates et al. 1996; Wong et al. 1999, 2010; Murphy et al. 2001; González-Davila 2003; Keeling et al. 2004; Midorikawa et al. 2006; Luger et al. 2006; Schuster and Watson 2007; Borges et al. 2008), in situ measurements are still insufficient in most parts of the

---

∂ Denotes Open Access content.

Corresponding author address: J. Zeng, CGER, National Institute for Environmental Studies, 16-2 Onogawa, Tsukuba, Ibaraki 305-8506, Japan.
E-mail: zeng@nies.go.jp

oceans because of technical and financial restrictions. This circumstance has motivated the search for robust and reliable methods to interpolate available CO_2 data spatially and temporally to obtain basinwide (e.g., Zeng et al. 2002; Lefèvre et al. 2005; Chierici et al. 2006; Sarma et al. 2006; Jamet et al. 2007; Friedrich and Oschlies 2009; Telszewski et al. 2009; Takamura et al. 2010; Landschützer et al. 2013; Nakaoka et al. 2013) and global ocean CO_2 maps (Takahashi et al. 2002, 2009). Conventional interpolation methods model CO_2 as a function of a number of biogeochemical variables. Recently, self-organizing maps (SOM), a type of artificial neural network, gained popularity in mapping the surface ocean CO_2 (Lefèvre et al. 2005; Friedrich and Oschlies 2009; Telszewski et al. 2009; Nakaoka et al. 2013; Landschützer et al. 2013). Using an artificial neural network differs distinctively from conventional statistical methods in that it is not required to formulate the model structure a priori.

In this work we introduce a new concept for mapping the surface ocean $f\mathrm{CO}_2$ (fugacity of CO_2) using a feed-forward neural network (FNN). As an artificial neural network, an FNN models and interpolates data nonlinearly, whereas a SOM establishes discrete estimates using a category map of limited size that associates a target variable with dependent variables (e.g., Telszewski et al. 2009). Previous studies applied a SOM to confined physical areas where biogeochemical variables were assumed to be able to interpret the $f\mathrm{CO}_2$ distribution well in a season. The concept is to exclude the temporal and spatial variables from the dependent variables of $f\mathrm{CO}_2$ so that scattered, multiple years' observations can be pooled together to train a neural network. The new concept of our model includes the dependence of $f\mathrm{CO}_2$ on time and space in the first place and considers biogeochemical variables as proxy variables for complementing insufficient observations. We gain two benefits from the new concept: (i) the model simulates observations faithfully where and when observations are sufficient and (ii) the monthly global climatology can be modeled by just one neural network.

2. Method

a. Model equations

Our analysis is based on a well-understood relationship stating that the $f\mathrm{CO}_2$ is a nonlinear function of time and space, which in our model are represented by month (MON), latitude (LAT), and longitude (LON), that is,

$$f\mathrm{CO}_2 = F(\mathrm{MON},\ \mathrm{LAT},\ \mathrm{LON}). \qquad (1)$$

Available observations are scarce with respect to the biogeochemical properties of the surface ocean; hence, a direct interpolation would include abnormally large uncertainties in many areas. One way to improve a direct interpolation is to include proxy variables that connect $f\mathrm{CO}_2$ variability with time and space to extend the model to unobserved areas. Following the works of Lefèvre et al. (2005), Friedrich and Oschlies (2009), Telszewski et al. (2009), Landschützer et al. (2013), and Nakaoka et al. (2013), we choose sea surface temperature (SST), sea surface salinity (SSS), and chlorophyll-*a* concentration (CHL) as proxy variables. Therefore, our basic model has the form of

$$f\mathrm{CO}_2 = F(\mathrm{MON},\ \mathrm{LAT},\ \mathrm{LON},\ \mathrm{SST},\ \mathrm{SSS},\ \mathrm{CHL}). \qquad (2)$$

We exclude the mixed layer depth (MLD) used by Telszewski et al. (2009), Nakaoka et al. (2013), and Landschützer et al. (2013), because openly available MLD data are scarce and our preliminary analysis using *World Ocean Atlas 1994* (*WOA94*) data (http://www.nodc.noaa.gov/OC5/WOA94/mix.html; Monterey and Levitus 1997) indicates that MLD (not shown here) has the least effect on $f\mathrm{CO}_2$ compared to SST, SSS, and CHL.

The MON and LON variables cannot be used directly because of their periodical properties. Therefore, we replaced each with two of its transformations, resulting in an updated model equation of the form

$$f\mathrm{CO}_2 = F(\mathrm{CMON},\ \mathrm{SMON},\ \mathrm{LAT},\ \mathrm{CLON},\ \mathrm{SLON},\ \mathrm{SST},\ \mathrm{SSS},\ \mathrm{CHL}), \qquad (3)$$

where

$$\mathrm{CMON} = \cos\left(\frac{\pi}{6}\mathrm{MON}\right),$$

$$\mathrm{SMON} = \sin\left(\frac{\pi}{6}\mathrm{MON}\right),$$

$$\mathrm{CLON} = \cos\left(\frac{\pi}{180}\mathrm{LON}\right), \quad \text{and}$$

$$\mathrm{SLON} = \sin\left(\frac{\pi}{180}\mathrm{LON}\right).$$

b. Neural network

Figure 1 illustrates the neural network used to model Eq. (3). It is a typical FNN having a layered structure and including three layers known as input, hidden, and output layers (Svozil et al. 1997). In our study, the input layer consists of eight neurons with one neuron corresponding to one independent variable in Eq. (3); the output layer has only one neuron whose output gives the scaled
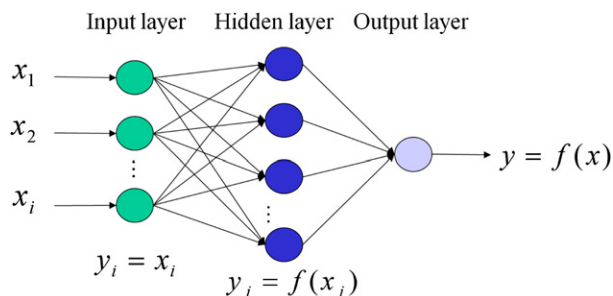
FIG. 1. The feed-forward neural network.

$f\text{CO}_2$; and the number of neurons in the hidden layer is empirically determined, which will be discussed later.

A neuron in the input layer takes the value of an independent variable and passes it to all neurons in the hidden layer without any transformation. A neuron in the hidden layer adds a bias to the weighted sum of all inputs (outputs from its upstream neurons in the input layer) and uses the transformed sum as an input for the output neuron, that is,

$$x = b + \sum_{i=1}^{M} w_i y_{i,\text{upstream}}$$
$$y = \frac{1}{1 + e^{-x}}, \tag{4}$$

in which M is the total number of input neurons. The neuron in the output layer transforms its inputs in the same way.

The sigmoid function is chosen because it increases monotonically from 0 to 1 for x from $-\infty$ to $+\infty$ and the derivative of y with respect to x has a simple form that affiliates the so-called error backpropagation algorithm (Rumelhart et al. 1986) for neural network training. The training algorithm adjusts the bias and weighting factors according to the negative gradient of the error cost function:

$$\mathbf{g} = \nabla E(\mathbf{w})$$
$$E(\mathbf{w}) = \frac{1}{2} \sum_{l=1}^{P} (d^l - y^l)^2, \tag{5}$$

in which P is the total number of training patterns (a pattern comprises a set of observations for $f\text{CO}_2$ and the proxy variables), y is the output of the FNN, and d is the target variable (i.e., the scaled $f\text{CO}_2$). We used the Levenberg–Marquardt method (Wilamowski and Yu 2010) to minimize the error cost function.

c. Neural network training

It is well known that, given a sufficiently large number of hidden neurons, an FNN can approximate any finite function (Hornik 1991; Blum and Li 1991). That indicates that if the $f\text{CO}_2$ values are unique in all training patterns

and correspond to unique values of MON, LAT, LON, SST, SSS, and CHL, Eq. (3) can be fitted accurately with a larger number of hidden neurons. An FNN configured as such remembers all training patterns and thus loses the capability of filtering out erroneous information in the source data. Unfortunately, there is no theoretically approved method for choosing the right number of hidden neurons (Svozil et al. 1997). Our criterion for selecting the number is that the standard deviation of the difference between model outputs and observations (std1) is no larger than the standard deviations of repeated $f\text{CO}_2$ observations averaged over all months and grid boxes (std2) by 20%, that is, |std1 − std2|/std2 < 0.2. At the experimental stage, we tried 4, 8, 16, 32, 64, and 128 hidden neurons. Eventually we settled on 32 according to the criterion.

d. Flux calculation

We further calculate the sea–air CO_2 flux as a function of the partial pressure of CO_2 ($p\text{CO}_2$) using

$$F = k_p(p\text{CO}_2^{\text{seawater}} - p\text{CO}_2^{\text{air}})$$
$$k_p = k_w k_0, \tag{6}$$

where k_p is the gas transfer coefficient, k_w is the gas transfer velocity, and k_0 is the solubility of CO_2 in seawater. We use the formulation of Wanninkhof (1992) for the coefficient k_w (cm h^{-1}) with the scaling factor of Takahashi et al. (2009); that is,

$$k_w = 0.26u^2(\text{Sc}/660)^{-0.5}, \tag{7}$$

where u (m s^{-1}) is the wind speed 10 m above the sea level and Sc is the Schmidt number, which varies with SST (°C; see Wanninkhof 1992):

$$\text{Sc} = 2073.1 - 125.62\text{SST} + 3.6276\text{SST}^2$$
$$- 0.043\,219\text{SST}^3. \tag{8}$$

The solubility k_0 (mol L^{-1} atm^{-1}) is a function of temperature T (K) = SST + 273.15 and SSS (Weiss 1974):

$$k_0 = -58.0931 + 90.5069(100/T)$$
$$+ 22.2940\ln(T/100) + \text{SSS}[0.027\,766$$
$$- 0.025\,888(T/100) + 0.005\,057\,8(T/100)^2]. \tag{9}$$

We multiply k_w by 7.03 to convert its unit to (m month^{-1}) and k_0 by 0.001 to convert its unit to (mol m^{-3} µatm^{-1}), so that Eq. (6) gives flux in (mol m^{-2} month^{-1}).

The conversion between $f\text{CO}_2$ and $p\text{CO}_2$ is done by the following formulation (see Weiss 1974):

$$f\text{CO}_2 = p\text{CO}_2 \exp\left(P_s \frac{B + 2\delta}{RT}\right), \tag{10}$$

where $R = 82.057\,46$ $(cm^3\,atm\,mol^{-1}\,K^{-1})$, P_s is the sea level air pressure used to substitute the equalibrator pressure, and B and δ are the virial coefficients for CO_2. Coefficient B $(cm^3\,mol^{-1})$ is given by

$$B = -1636.75 + 12.0408T - 3.279\,57e^{-2}T^2$$
$$+ 3.165\,28e^{-5}T^3 \tag{11}$$

and δ $(cm^3\,mol^{-1})$ by

$$\delta = 57.7 - 0.118T. \tag{12}$$

3. Data

a. CO_2 data

We extracted monthly $f\mathrm{CO}_2$ data from the track-gridded database of the Surface Ocean CO_2 Atlas (SOCAT) version 2.0 (http://www.socat.info/; Pfeil et al. 2013; Sabine et al. 2013; Bakker et al. 2013). The database has a $1° \times 1°$ spatial resolution and includes global measurements from 1970 to 2011. We excluded some data points using four criteria: (i) year before 1990, (ii) $f\mathrm{CO}_2$ values smaller than 200 μatm or larger than 600 μatm, (iii) ocean depth smaller than 1000 m, and (iv) salinity smaller than 30.0. The first criterion is for reducing the uncertainty of normalizing $f\mathrm{CO}_2$ to the reference year of 2000 for comparison with the global CO_2 maps of Takahashi et al. (2009). The second criterion is for reducing the potential effect of extreme data points on the extrapolation of the FNN. The last two criteria are for identifying seawater in open oceans.

We obtained 127 880 data points or patterns from multiple years' data for training the FNN to estimate the global mean increase rate of $f\mathrm{CO}_2$. The rate was then used to normalize multiple years' $f\mathrm{CO}_2$ to obtain the monthly $f\mathrm{CO}_2$ climatology, which comprises the means of repeated observations in the same months and same grid boxes. From the climatology, we obtained 73 265 data points for training the FNN to model the global $f\mathrm{CO}_2$ climatology. Figure 2 shows the composite sampling map of SOCAT in 1990–2011.

We prepared more CO_2 data for training the FNN to evaluate the difference between the results of the FNN and Takahashi et al. (2009). In addition to the four criteria, we excluded data points in the equatorial Pacific, 10°N–10°S, in the El Niño periods, which were selected according to the National Oceanic and Atmospheric Administration (NOAA)'s analysis (http://www.cpc.ncep.noaa.gov/products/analysis_monitoring/ensostuff/ensoyears.shtml), resulting in 71 287 data points. Unless specifically stated in latter discussions, our FNN model
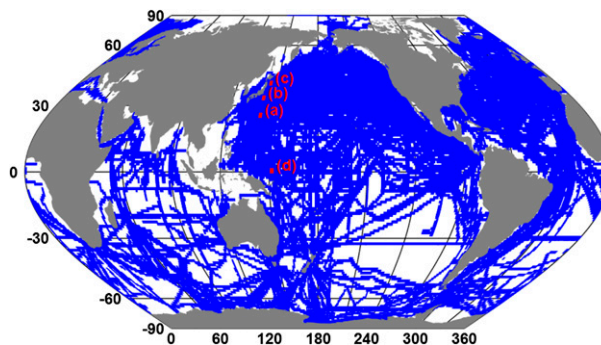

FIG. 2. Sampling map of all observations included in the SOCAT version 2.0 database. (a)–(d) Observations in grid boxes are used in Fig. 5 to compare observed and modeled seasonal variations.

results refer to those obtained by using the first CO_2 dataset.

b. Proxy variable data

The monthly SST data of 1990–2011 were extracted from the NOAA optimum interpolation (OI) version 2 product (http://www.esrl.noaa.gov/psd/data/gridded/data.noaa.oisst.v2.html; Reynolds et al. 2002). We calculated the SST climatology using SST in that period. The SSS climatology was extracted from the *World Ocean Atlas 2009* (*WOA09*) product (http://www.nodc.noaa.gov/OC5/WOA09/netcdf_data.html; Antonov et al. 2010). The *WOA09* SSS covers the period of June 1890–December 2008. The CHL climatology was calculated using the Moderate Resolution Imaging Spectroradiometer (MODIS) *Aqua* and Sea-viewing Wide Field-of-view Sensor (SeaWiFS) climatology (http://oceancolor.gsfc.nasa.gov/cgi/l3). The 9-km gridded satellite data were binned into $1° \times 1°$ grid boxes. The mean of the two CHLs was used as the CHL climatology for our model. At the time we obtained the data, *Aqua* CHL covers the period of July 2002–July 2013 and SeaWiFS CHL from September 1997 to December 2010.

c. Data for flux calculation

The required monthly wind speed and air pressure were calculated using the National Centers for Environmental Prediction Final Operational Global Analysis (NCEP-FNL) data (http://rda.ucar.edu/datasets/ds083.2/) of the years 2000–11, as the data before July 1999 are unavailable. The product has a spatial resolution of $1° \times 1°$ and a temporal resolution of 6 h. We used the atmospheric $p\mathrm{CO}_2$ in the database (http://www.ldeo.columbia.edu/res/pi/CO2/) of Takahashi et al. (2009) in order to compare with their flux results. For estimating the global flux, we filled our unmodeled grid boxes, in which CHL is unavailable, using their seawater $p\mathrm{CO}_2$ values. The unmodeled area size is about 6% of our modeled area size.

d. Data scaling

Equation (4) indicates that data used as input can take any real values. However, an FNN usually initializes bias and weight parameters randomly in a predetermined range for generalizing its use with all kinds of inputs; therefore, scaling input data speeds up the convergence within the training process. We scale the values v of an input variable by their mean and standard deviation σ as

$$v' = \frac{v - \overline{v}}{\sigma}, \tag{13}$$

so that they have a zero mean and a standard deviation of one. The observed $f\mathrm{CO}_2$ is scaled using

$$v' = 0.1 + 0.8 \frac{v - v_{\min}}{v_{\max} - v_{\min}}. \tag{14}$$

This confines the scaled $f\mathrm{CO}_2$ to between 0.1 and 0.9. The reason for the confinement is that Eq. (4) results in y values within the range of 0–1 and that a small change in y near zero or one requires a very large change in x, which will slow the convergence of training.

Before being scaled by Eq. (13), chlorophyll is transform by

$$v' = \log_{10}(1 + v). \tag{15}$$

The transformation helps to reduce the strongly skewed CHL values; that is, a majority number of CHL values are very small. The skewed distribution potentially leads to a trained FNN to have neuron parameters more optimized toward fitting small CHL well, thus weakening its prediction power for large CHL.

4. Results and discussions

a. CO$_2$ increase rate

As the surface ocean CO_2 concentration varies in responding to changes in biogeochemical conditions and to the increase of atmospheric CO_2 concentration, the increase rate of the surface ocean CO_2 showed geographical differences (see the summary in Takahashi et al. 2009). A constant CO_2 increase rate was usually used to normalize multiple years' CO_2 data to a reference year (e.g., Takahashi et al. 2009; Nakaoka et al. 2013). Instead of adopting an available rate for our $f\mathrm{CO}_2$ data normalization, we used the FNN to estimate the global mean rate by repeating the following procedures until the error in Eq. (5) became stable: (i) modeling Eq. (3) with the $f\mathrm{CO}_2$ and SST of 1990–2011 and the climatology of SSS and CHL; (ii) linearly fitting the difference
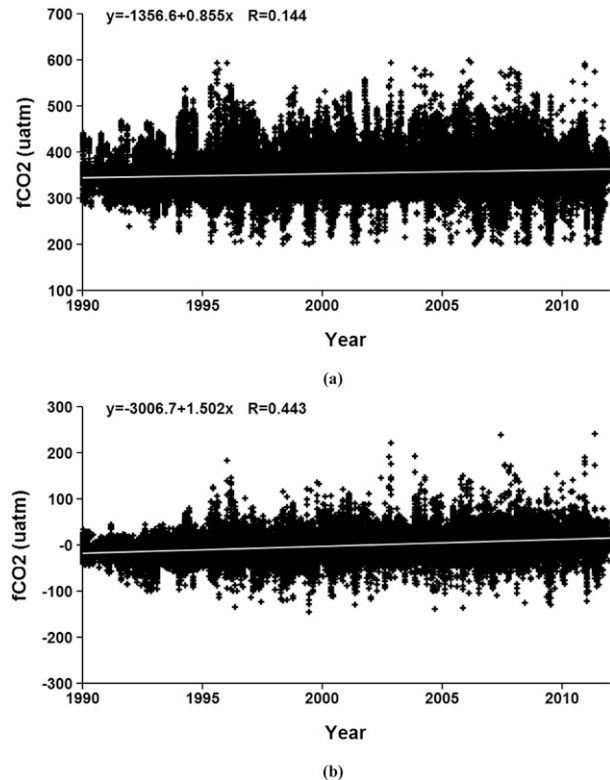

FIG. 3. Linear fit of $f\mathrm{CO}_2$ against time. (a) Fitting the observed $f\mathrm{CO}_2$ with time yielded an increase rate of 0.855 μatm yr^{-1} and a correlation coefficient of 0.144. (b) Fitting the $f\mathrm{CO}_2$ difference (observation $-$ model) yielded an increase rate of 1.502 μatm yr^{-1} and a correlation coefficient of 0.443. The trend was enhanced because of the subtraction of modeled seasonal and spatial variability.

between the modeled and observed $f\mathrm{CO}_2$ against time (year) to estimate the annual increase rate; and (iii) adjusting the observed $f\mathrm{CO}_2$ by the rate and then going to procedure (i) with the adjusted $f\mathrm{CO}_2$ as the target.

The procedures are equivalent to treating the $f\mathrm{CO}_2$ increase rate as an error term in the FNN modeling and treating the seasonal and spatial variations of $f\mathrm{CO}_2$ as an error term in linear fitting. By recursively trying to guess the variations, removing the variations to guess the trend, and detrending the observed $f\mathrm{CO}_2$ to guess the variations again, the procedures effectively reduced the seasonal and spatial variations of CO_2 in the residue. As a result, the trend signal became stronger with the increasing number of iterations. At first, a direct linear fit of the observed $f\mathrm{CO}_2$ resulted in a rate of 0.855 μatm yr^{-1} and a correlation coefficient of 0.144. After the first recursion, the FNN improved the correlation to 0.332 and gave a global mean rate of 1.085 μatm yr^{-1}. The magnitude of improvement decreased with the number of iterations. The mean FNN error became stable after repeating procedures (i) to (iii) 5 times. Finally, the FNN gave a rate
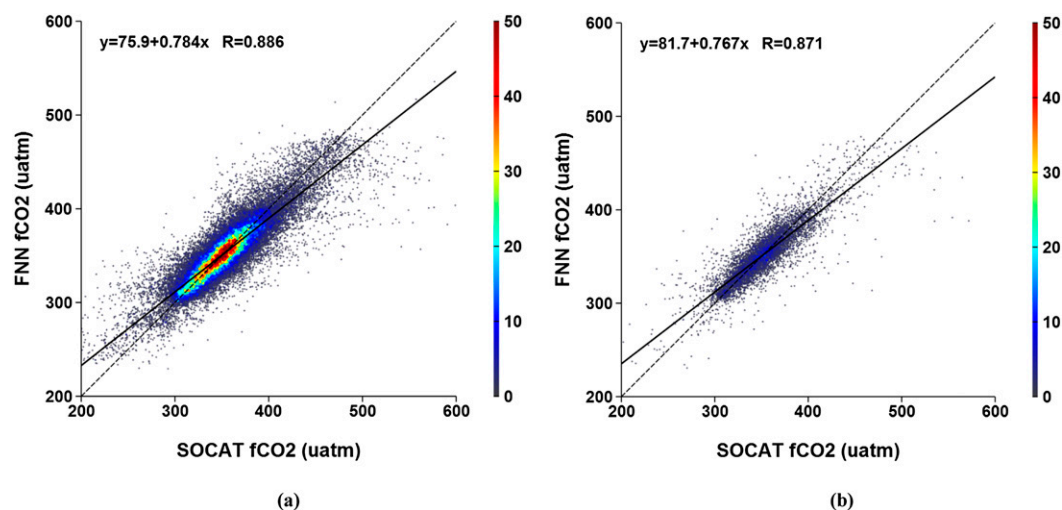
FIG. 4. Modeled $f\mathrm{CO_2}$ vs observed $f\mathrm{CO_2}$. (a) Fitting for the training samples yielded a slope of 0.785 and a correlation coefficient of 0.886. (b) Fitting for validation samples yielded a slope of 0.776 and a correlation coefficient of 0.883. The solid line is the linear regression line, and the dashed line is the line of slope 1 passing through the origin. The color bar indicates the number of points in $1° \times 1°$ grid boxes.

of $1.502\,\mu\mathrm{atm\,yr^{-1}}$ and a correlation coefficient of 0.443 (Fig. 3). The stabled increase rate is consistent with previously used values (e.g., Takahashi et al. 2009).

b. Nonlinear fitting

The annual increase rate of $1.502\,\mu\mathrm{atm\,yr^{-1}}$ was used to normalize monthly $f\mathrm{CO_2}$ of 1990–2011 to the reference year 2000. The FNN was further trained by using the normalized $f\mathrm{CO_2}$ and the climatology of SST, SSS, and CHL. To evaluate the predictive performance, we randomly took 90% of the 73 265 patterns for training use and the remaining 10% for validation. By using a different random seed, we could test cases with different subsamples. The results are all similar to those shown in Fig. 4. The linear regression of modeled $f\mathrm{CO_2}$ versus observed $f\mathrm{CO_2}$ in the training samples gives a slope of 0.784 and a correlation coefficient of $R = 0.886$. The mean and standard deviation of the bias (FNN – SOCAT) are -0.01 and $15.8\,\mu\mathrm{atm}$, respectively. Considering the mean standard deviation of repeated observations of $13.2\,\mu\mathrm{atm}$, these values indicate that the bias is negligibly small and that the FNN models the nonlinear relationship of Eq. (3) well. For the validation subsamples, the slope and correlation coefficient are 0.767 and 0.871, respectively; and the mean and standard deviation of the bias are -0.16 and $16.0\,\mu\mathrm{atm}$, respectively. The validation results further indicate that the FNN model is acceptable for interpolating $f\mathrm{CO_2}$ to unsampled areas. Finally, we used all samples to train the FNN in order to produce global $f\mathrm{CO_2}$ maps. It yields a slope of 0.778, a correlation coefficient of 0.882, and a mean and standard deviation of the bias of -0.01 and $15.4\,\mu\mathrm{atm}$, respectively.

Including space and time variables in the model yields a good representation of the seasonal cycle of $f\mathrm{CO_2}$. Figure 5 shows four examples for the western Pacific near the meridian line of 145°E, where the volunteer cargo ship observation of the National Institute for Environmental Studies supplies every monthly observation data (Nakaoka et al. 2013). They reveal three seasonal patterns shared by other oceans: (i) temperature-driven seasonality of low $f\mathrm{CO_2}$ in winter and high $f\mathrm{CO_2}$ in summer (Fig. 5a), (ii) $f\mathrm{CO_2}$ drawdown by biological activities from spring to summer (Fig. 5b), and (iii) second $f\mathrm{CO_2}$ drawdown by biological activities in autumn (Fig. 5c). In many areas in the tropical zone from about 20°S to 20°N, persistently high temperature, and low biological activity lead to less pronounced seasonal changes with high fluctuations (Fig. 5d). The coupling of $\mathrm{CO_2}$ variability with temperature and biological activities is in good agreement with previous findings (e.g., Bates 2001; Takahashi et al. 2002; Zeng et al. 2002).

c. Comparisons

For the convenience of discussion, we use FNN1 and FNN2 to represent the FNN trained with and without data points in the El Niño periods (see section 3b), respectively. Similarly, we use OBS1 for SOCAT observations normalized to the year 2000 and OBS2 for the same data but without data points in the El Niño periods. And we use the name T09 for the Lamont–Doherty Earth Observatory (LDEO) climatology of Takahashi et al. (2009), who interpolated the monthly $p\mathrm{CO_2}$ to obtain global distributions based on a lateral, two-dimensional advection–diffusion transport for surface ocean. The distributions of the annual
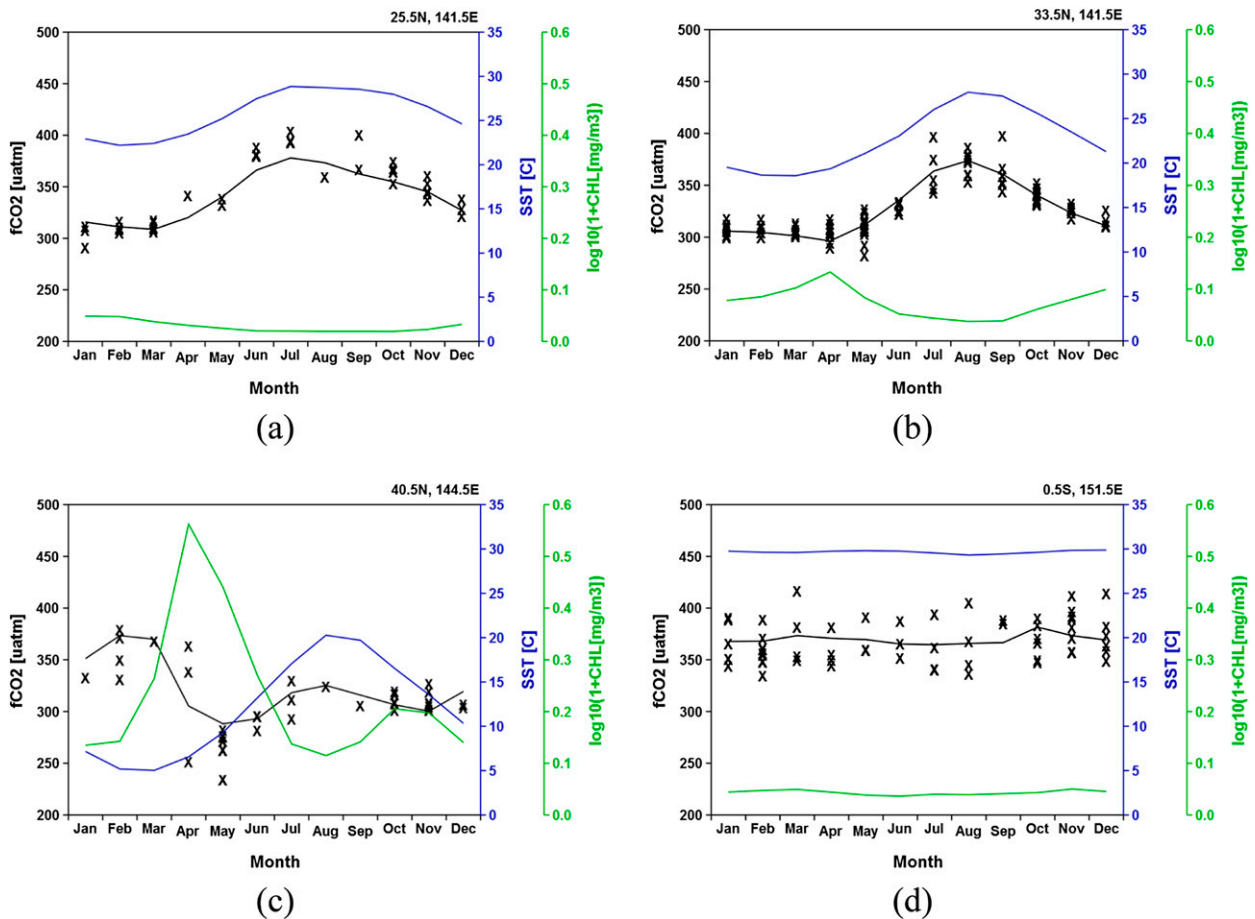
FIG. 5. Seasonal changes of modeled (dark line) and observed (cross symbol) fCO$_2$, sea surface temperature (blue line), and chlorophyll-a (green line). (a)–(d) Positions of the panels are shown in Fig. 2.

mean of fCO$_2$ difference among models and observations are shown in Fig. 6. Monthly statistics of the fCO$_2$ differences are listed in Table 1.

Our model results show small monthly-mean biases (within 1.5 μatm) compared to the observations (Table 1). The overall bias of both FNN1 and FNN2 is zero. The T09 results also show small monthly-mean biases (within 1.1 μatm), but a small negative overall bias (0.4 μatm) and a larger overall uncertainty (17.5 μatm) compared with FNN1 and FNN2 (15.4 μatm). Between FNN2 and T09, small monthly-mean differences (within 0.5 μatm) occur in April, November, and December (Table 1). Relatively large monthly-mean differences (up to 4.2 μatm) occur in other months. Annually, the mean difference is about 0.9 $\pm$ 15.8 μatm.

Large differences between FNN2 and T09 occur near the equator and in areas where observations are relatively scarce (Fig. 6a). Compared to the observations, large differences seem to be associated with undersampling and large CHL uncertainty for the FNN and the T09 models (Figs. 6b,c). As shown in Fig. 5d,

the observed fCO$_2$ in the tropical area includes large variability throughout the year, while the amplitude of the seasonal variation is relatively small. As a result, both the FNN2 and T09 models show relatively large differences against OBS in the equatorial areas (Figs. 6b,c).

We put both modeled and observed fCO$_2$ for September, when the T09−FNN2 difference is the largest, in Fig. 7. The T09−FNN2 difference fluctuates at the basin scale in most areas (Fig. 7a). T09 shows particularly high fCO$_2$ unlike FNN2 in the zone near 30°S and near the Antarctic. By comparing both models' results (Figs. 7b,c) with the observations (Fig. 7d), it becomes clear that a large T09−FNN2 difference is likely caused by T09's overestimation and FNN2's underestimation. In contrast, the T09 fCO$_2$ is generally smaller than the FNN2 fCO$_2$ in the equatorial areas. We attribute the discrepancy to the model uncertainty caused by relatively large fCO$_2$ fluctuation in the same month.

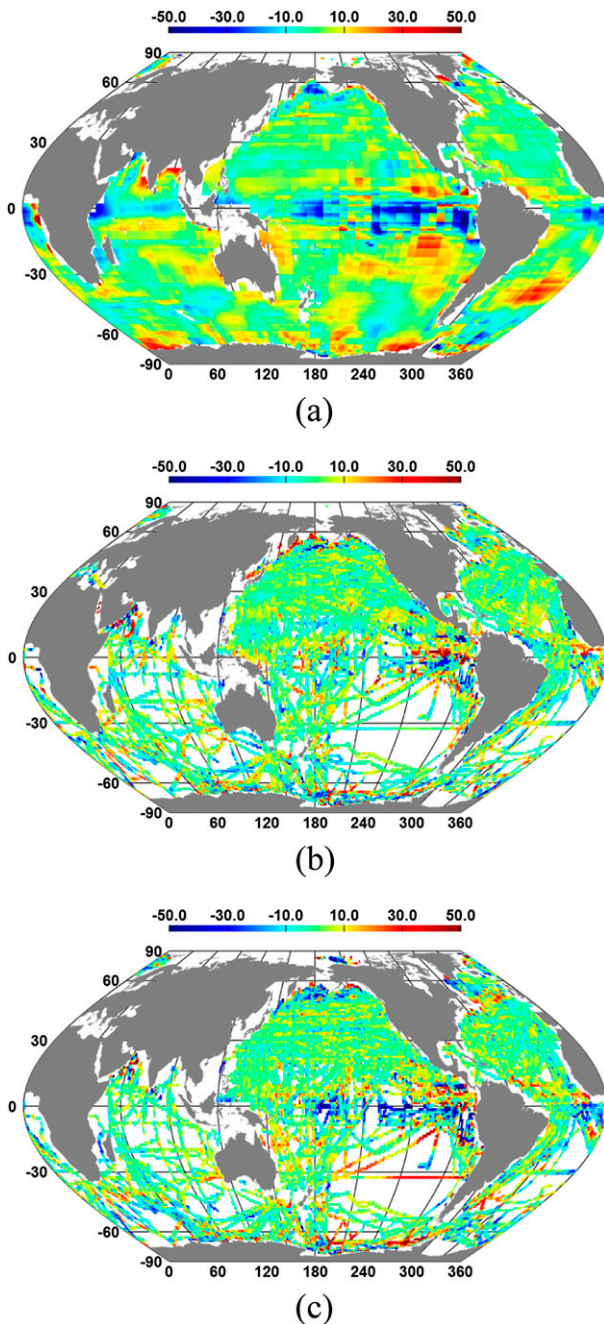Nevertheless, both the FNN and T09 models yield results that agree generally well with observations

FIG. 6. Distribution of annual mean differences of fCO$_2$ among models and observations: (a) T09 − FNN2, (b) FNN2 − OBS2, and (c) T09 − OBS2. Both FNN2 and OBS2 do not include data points in the El Niño periods.

throughout the year (Fig. 8). Our monthly climatology maps, which include El Niño data points, illustrate clear seasonal fCO$_2$ variations. The FNN product has the benefit of a finer spatial resolution compared to the T09 product, but it has the disadvantage of larger areas of missing data because of missing CHL inputs.

We evaluated the uncertainty of the FNN caused by using different proxy variable data. As the evaluation on a second dataset did not meaningfully change the conclusions, the results are not shown here.

d. CO$_2$ flux

The gas transfer coefficient k_p in Eq. (6) is primarily a function of wind speed (Takahashi et al. 2009); hence, the flux calculation can differ significantly depending on the wind product used. By applying the wind speed from a different wind product to the pCO$_2$ of T09, Wanninkhof et al. (2013) yielded a global sea–air CO$_2$ flux of −1.18 PgC yr^{-1}, which is 15% less negative than that of T09 (−1.38 PgC yr^{-1}). Using the wind and pCO$_2$ data of T09, our formulation also yields a global air–sea CO$_2$ flux of −1.39 PgC yr^{-1} even though different SST and SSS data were used (Table 2). However, when the T09 wind was replaced by the NCEP–FNL wind (see section 3c), we yielded a global flux of −1.04 PgC yr^{-1} for the T09 pCO$_2$, which is about 25% less negative. Being aware of this uncertainty, we present our flux estimate as the range resulting from both wind data. For comparison reasons, we filled 6% of the areas, where there were no direct estimates from the FNN, by T09 CO$_2$ data to estimate the CO$_2$ flux in this study. Fluxes thus calculated are summarized in Table 2.

Overall, our results suggest a global sea–air CO$_2$ flux ranging from −1.31 to −1.66 PgC yr^{-1} by including the El Niño periods (FNN1) and from −1.22 to −1.57 PgC yr^{-1} by excluding those periods (FNN2). They are about 15%–25% more negative than the estimate in T09 when the same wind product is used. Averaging zonally, the Southern Ocean south of 20°S contributes the most (about −1.17 PgC yr^{-1}) to the total flux, while the northern oceans north of 20°N contribute roughly two-thirds the amount (about −0.75 PgC yr^{-1}). In contrast, the equatorial zone from 20°S to 20°N appears to be a prominent source with a net flux of 0.61 PgC yr^{-1}. The relative zonal contributions agree well with the numbers obtained by Takahashi et al. (2009).

As the FNN uncertainty caused by data points in the El Niño periods is small, we report our model flux based on the FNN1 results. By adding a correction of −0.2 PgC yr^{-1} for undersampling (Wanninkhof et al. 2013) to the direct estimate, we obtain a net annual CO$_2$ uptake of −1.5 to −1.9 PgC yr^{-1} for the global ocean. Furthermore, by including an estimate for the riverine CO$_2$ flux of 0.4 PgC yr^{-1} to the oceans (e.g., Jacobson et al. 2007), we yield an anthropogenic CO$_2$ uptake of −1.9 to −2.3 PgC yr^{-1}. These values are in good agreement with the best estimate for the anthropogenic CO$_2$ uptake by Wanninkhof et al. (2013).

TABLE 1. Monthly differences of fCO_2 (μatm) among models and observations. The range is the mean standard deviation of differences in grid boxes.

Month	FNN1 − OBS1	FNN2 − OBS2	T09 − OBS2	T09 − FNN2
Jan	−0.8 ± 16.6	−0.1 ± 16.6	−0.8 ± 18.1	−1.8 ± 16.6
Feb	1.1 ± 15.2	1.3 ± 15.1	−0.2 ± 16.8	−2.2 ± 16.2
Mar	−0.0 ± 14.9	−1.2 ± 15.7	−1.3 ± 16.9	−1.3 ± 15.5
Apr	−0.5 ± 14.0	−0.6 ± 14.2	−0.6 ± 16.9	0.5 ± 14.0
May	−0.5 ± 15.5	0.2 ± 14.6	−0.3 ± 17.2	1.3 ± 15.7
Jun	1.0 ± 16.9	1.5 ± 17.3	−1.0 ± 20.0	1.5 ± 16.6
Jul	0.5 ± 15.7	−0.2 ± 15.8	1.1 ± 17.9	3.6 ± 16.6
Aug	−0.5 ± 15.8	−0.9 ± 16.0	−0.4 ± 17.2	3.4 ± 16.5
Sep	−1.0 ± 14.3	−0.3 ± 14.2	−0.2 ± 15.8	4.2 ± 16.6
Oct	0.3 ± 14.8	0.3 ± 14.4	−0.0 ± 16.9	2.2 ± 14.4
Nov	1.3 ± 14.8	0.8 ± 15.1	−0.8 ± 17.9	0.5 ± 13.9
Dec	−1.2 ± 15.8	−1.2 ± 15.7	−0.2 ± 18.1	0.4 ± 15.9
Avg	−0.0 ± 15.4	−0.0 ± 15.4	−0.4 ± 17.5	0.9 ± 15.8
No. points	73 265	71 287	71 917	346 351

5. Conclusions

Our global fCO_2 climatology derived from a feed-forward neural network, including the time and space variables, reveals a great potential to produce an fCO_2 product for the modeling community. The model generally simulates the seasonal variation of fCO_2 well and yields monthly distributions that are in good agreement with observations. Our product also agrees well with the LDEO product (Takahashi et al. 2009), but it
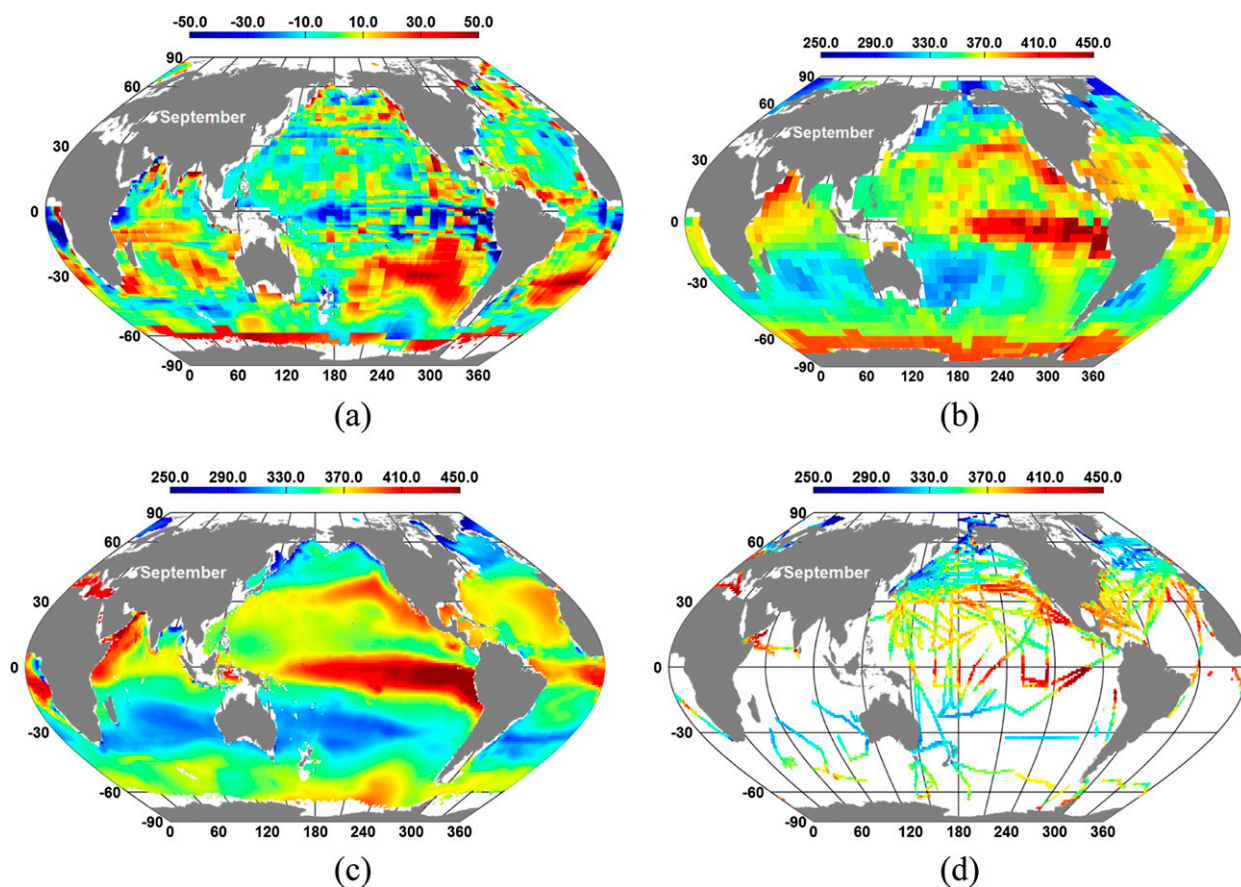

FIG. 7. Comparison between models and observations for September: (a) T09–FNN2 fCO_2 difference, (b) T09 fCO_2 distribution, (c) FNN2 fCO_2 distribution, and (d) OBS2 distribution.
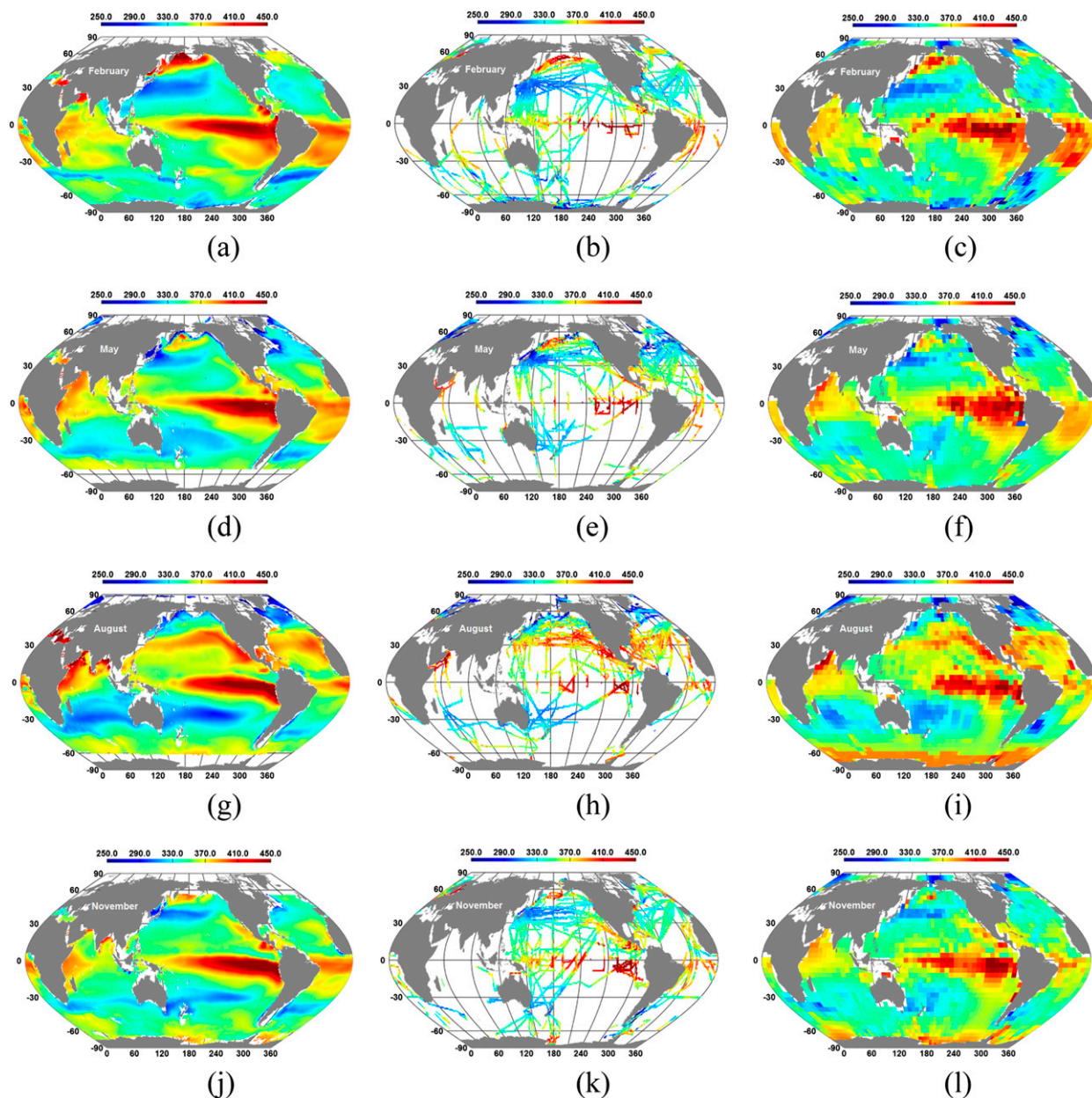
FIG. 8. Distributions of fCO$_2$ in February, May, August, and November. (a),(d),(g),(j) The FNN1 maps exclude areas when and where CHL was not available. (b),(e),(h),(k) The OBS1 maps include all the points extracted on the conditions discussed in section 3a. (c),(f),(i),(l) The T09 maps have a $4° \times 5°$ spatial resolution and exclude data from El Niño years. (The FNN model results can be downloaded from http://db.cger.nies.go.jp/ged/Open-Data/JTECH-D-13-00137/.)

has a much higher spatial resolution. Our method has the advantage of not having to define a fixed model relationship between fCO$_2$ and its dependent variables. Its advantage over the SOM method (e.g., Telszewski et al. 2009) is that the interpolation of fCO$_2$ is continuous, whereas an SOM establishes discrete estimates using a category map. Regarding the method of Landschützer et al. (2013) that uses both SOM and FNN, our method is much simpler in that only one neural network configuration is sufficient to model the global fCO$_2$ in all seasons, whereas Landschützer et al. (2013) focused their method on the interannual variability of the Atlantic Ocean carbon sink. We achieved this by including transformed time and space as input parameters. The model is robust and can be extended to produce global fCO$_2$ with a higher resolution in time and space as long as required data for input variables are available.

TABLE 2. Global and zonal CO_2 fluxes (PgC yr^{-1}) obtained by using wind products of NCEP FNL and NCEP Reanalysis (RNL) in the T09 database.

Model	Global (FNL)	Global (RNL)	North of 10°N (FNL)	20°N–20°S (FNL)	South of 20°S (FNL)
FNN1	−1.31	−1.66	−0.75	0.61	−1.17
FNN2	−1.22	−1.57	−0.75	0.66	−1.14
T09	−1.04	−1.39	−0.78	0.67	−0.94

Our anthropogenic CO_2 uptake estimate agrees well with the best estimate of Wanninkhof et al. (2013), but it appears to be about 15%–25% larger than the estimate of Takahashi et al. (2009). The uncertainty caused by including or excluding data in the El Niño periods is small compared to the difference between models. The difference caused by using different wind products can be as large as the difference between models and provides the largest CO_2 flux uncertainty of our method.

REFERENCES

Antonov, J. I., D. Seidov, T. P. Boyer, R. A. Locarnini, A. V. Mishonov, and H. E. Garcia, 2010. *Salinity.* Vol. 2, *World Ocean Atlas 2009,* NOAA Atlas NESDIS 69, 184 pp.

Bakker, D. C. E., and Coauthors, 2013: An update to the Surface Ocean CO_2 Atlas (SOCAT version 2). *Earth Syst. Sci. Data Discuss.,* **6,** 465–512, doi:10.5194/essdd-6-465-2013.

Bates, N. R., 2001: Interannual variability of oceanic CO_2 and biogeochemical properties in the western North Atlantic subtropical gyre. *Deep-Sea Res. II,* **48,** 1507–1528, doi:10.1016/S0967-0645(00)00151-X.

——, A. F. Michaels, and A. H. Knap, 1996: Seasonal and interannual variability of oceanic carbon dioxide species at the U.S. JGOFS Bermuda Atlantic Time-Series Study (BATS) site. *Deep-Sea Res. II,* **43,** 347–383, doi:10.1016/0967-0645(95)00093-3.

Blum, E. K., and L. K. Li, 1991: Approximation theory and feedforward networks. *Neural Networks,* **4,** 511–515, doi:10.1016/0893-6080(91)90047-9.

Borges, A. V., B. Tilbrook, N. Metzl, A. Lenton, and B. Delille, 2008: Inter-annual variability of the carbon dioxide oceanic sink south of Tasmania. *Biogeosciences,* **5,** 141–155, doi:10.5194/bg-5-141-2008.

Chierici, M., A. Fransson, and Y. Nojiri, 2006: Biogeochemical processes as drivers of surface fCO_2 in contrasting provinces in the subarctic North Pacific Ocean. *Global Biogeochem. Cycles,* **20,** GB1009, doi:10.1029/2004GB002356.

Cooper, D. J., A. J. Watson, and R. D. Ling, 1998: Variation of pCO_2 along a North Atlantic shipping route (U.K. to the Caribbean): A year of automated observations. *Mar. Chem.,* **60,** 147–164, doi:10.1016/S0304-4203(97)00082-0.

Feely, R. A., R. H. Gammon, B. A. Taft, P. E. Pullen, L. S. Waterman, T. J. Conway, J. F. Gendron, and D. P. Wisegarver, 1987: Distribution of chemical tracers in the eastern equatorial Pacific during and after the 1982–1983 El Nino/Southern Oscillation event. *J. Geophys. Res.,* **92,** 6545–6558, doi:10.1029/JC092iC06p06545.

Friedrich, T., and A. Oschlies, 2009: Neural network-based estimates of North Atlantic surface pCO_2 from satellite data: A methodological study. *J. Geophys. Res.,* **114,** C03020, doi:10.1029/2007JC004646.

González-Davila, M., J. M. Santana-Casiano, M. J. Rueda, O. Llinás, and E. F. González-Dávila, 2003: Seasonal and interannual variability of sea-surface carbon dioxide species at the European Station for Time Series in the Ocean at the Canary Islands (ESTOC) between 1996 and 2000. *Global Biogeochem. Cycles,* **17,** 1076, doi:10.1029/2002GB001993.

Gruber, N., and Coauthors, 2009: Oceanic sources, sinks, and transport of atmospheric CO_2. *Global Biogeochem. Cycles,* **23,** GB1005, doi:10.1029/2008GB003349.

Hornik, K., 1991: Approximation capabilities of multilayer feedforward networks. *Neural Networks,* **4,** 251–257, doi:10.1016/0893-6080(91)90009-T.

Inoue, H. Y., H. Matsueda, M. Ishii, K. Fushimi, M. Hirota, I. Asanuma, and Y. Takasugi, 1995: Long-term trend of the partial pressure of carbon-dioxide (pCO_2) in surface waters of the western North Pacific, 1984–1993. *Tellus,* **47B,** 391–413, doi:10.1034/j.1600-0889.47.issue4.2.x.

Jacobson, A. R., S. E. Mikaloff Fletcher, N. Gruber, J. L. Sarmiento, and M. Gloor, 2007: A joint atmosphere-ocean inversion for surface fluxes of carbon dioxide: 1. Methods and global-scale fluxes. *Global Biogeochem. Cycles,* **21,** GB1019, doi:10.1029/2005GB002556.

Jamet, C., C. Moulin, and N. Lefèvre, 2007: Estimation of the oceanic pCO_2 in the North Atlantic from VOS lines in-situ measurements: Parameters needed to generate seasonally mean maps. *Ann. Geophys.,* **25,** 2247–2257, doi:10.5194/angeo-25-2247-2007.

Keeling, C. D., H. Brix, and N. Gruber, 2004: Seasonal and long-term dynamics of the upper ocean carbon cycle at Station ALOHA near Hawaii. *Global Biogeochem. Cycles,* **18,** GB4006, doi:10.1029/2004GB002227.

Komhyr, W. D., R. H. Gammon, T. B. Harris, L. S. Waterman, T. J. Conway, W. R. Taylor, and K. W. Thoning, 1985: Global atmospheric CO_2 distribution and variations from 1968–1982 NOAA/GMCC CO_2 flask sample data. *J. Geophys. Res.,* **90,** 5567–5596, doi:10.1029/JD090iD03p05567.

Landschützer, P., N. Gruber, D. C. E. Bakker, U. Schuster, S. Nakaoka, M. R. Payne, T. Sasse, and J. Zeng, 2013: A neural network-based estimate of the seasonal to inter-annual variability of the Atlantic Ocean carbon sink. *Biogeosci. Discuss.,* **10,** 8799–8849, doi:10.5194/bgd-10-8799-2013.

Lefèvre, N., A. J. Watson, and A. R. Watson, 2005: A comparison of multiple regression and neural network techniques for mapping *in situ* pCO_2 data. *Tellus,* **57B,** 375–384, doi:10.1111/j.1600-0889.2005.00164.x.

Luger, H., R. Wanninkhof, D. W. R. Wallace, and A. Körtzinger, 2006: CO_2 fluxes in the subtropical and subarctic North Atlantic based on measurements from a volunteer observing ship. *J. Geophys. Res.,* **111,** C06024, doi:10.1029/2005JC003101.

Midorikawa, T., and Coauthors, 2006: Interannual variability of winter oceanic CO_2 and air-sea CO_2 flux in the western North Pacific for 2 decades. *J. Geophys. Res.,* **111,** C07S02, doi:10.1029/2005JC003095.

Monterey, G., and S. Levitus, 1997: *Seasonal Variability of Mixed Layer Depth for the World Ocean.* NOAA Atlas NESDIS 14, 96 pp.

Murphy, P. P., Y. Nojiri, Y. Fujinuma, C. S. Wong, J. Zeng, T. Kimoto, and H. Kimoto, 2001: Measurements of surface seawater fCO_2 from volunteer commercial ships: Techniques and experiences from *Skaugran. J. Atmos. Oceanic Technol.,* **18,** 1719–1734, doi:10.1175/1520-0426(2001)018<1719:MOSSFC>2.0.CO;2.

Nakaoka, S., M. Telszewski, Y. Nojiri, S. Yasunaka, C. Miyazaki, H. Mukai, and N. Usui, 2013: Estimating temporal and spatial variation of ocean surface pCO_2 in the North Pacific using a self-organizing map neural network technique. *Biogeosciences,* **10,** 6093–6106, doi:10.5194/bg-10-6093-2013.

Pfeil, B., and Coauthors, 2013: A uniform, quality controlled Surface Ocean CO_2 Atlas (SOCAT). *Earth Syst. Sci. Data,* **5,** 125–143, doi:10.5194/essd-5-125-2013.

Reynolds, R. W., N. A. Rayner, T. M. Smith, D. C. Stokes, and W. Wang, 2002: An improved in situ and satellite SST analysis for climate. *J. Climate,* **15,** 1609–1625, doi:10.1175/1520-0442(2002)015<1609:AIISAS>2.0.CO;2.

Rumelhart, D. E., G. E. Hinton, and R. J. Williams, 1986: Learning representations by back-propagating errors. *Nature,* **323,** 533–536, doi:10.1038/323533a0.

Sabine, C. L., and Coauthors, 2004: The oceanic sink for anthropogenic CO_2. *Science,* **305,** 367–371, doi:10.1126/science.1097403.

——, and Coauthors, 2013: Surface Ocean CO_2 Atlas (SOCAT) gridded data products. *Earth Syst. Sci. Data,* **5,** 145–153, doi:10.5194/essd-5-145-2013.

Sarma, V. V. S. S., T. Saino, K. Sasaoka, Y. Nojiri, T. Ono, M. Ishii, H. Y. Inoue, and K. Matsumoto, 2006: Basin-scale pCO_2 distribution using satellite sea surface temperature, Chl *a,* and climatological salinity in the North Pacific in spring and summer. *Global Biogeochem. Cycles,* **20,** GB3005, doi:10.1029/2005GB002594.

Schuster, U., and A. J. Watson, 2007: A variable and decreasing sink for atmospheric CO_2 in the North Atlantic. *J. Geophys. Res.,* **112,** C11006, doi:10.1029/2006JC003941.

Svozil, D., V. Kvasnicka, and J. Pospichal, 1997: Introduction to multi-layer feed-forward neural networks. *Chemom. Intell. Lab. Syst.,* **39,** 43–62, doi:10.1016/S0169-7439(97)00061-0.

Takahashi, T., and Coauthors, 2002: Global sea–air CO_2 flux based on climatological surface ocean pCO_2, and seasonal biological and temperature effects. *Deep-Sea Res. II,* **49,** 1601–1622, doi:10.1016/S0967-0645(02)00003-6.

——, and Coauthors, 2009: Corrigendum to ''Climatological mean and decadal change in surface ocean pCO_2, and net sea–air CO_2 flux over the global oceans'' [Deep Sea Res. II 56 (2009) 554–577]. *Deep-Sea Res. I,* **56,** 2075–2076, doi:10.1016/j.dsr.2009.07.007.

Takamura, T. R., H. Y. Inoue, T. Midorikawa, M. Ishii, and Y. Nojiri, 2010: Seasonal and inter-annual variations in pCO_2^{sea} and air-sea CO_2 fluxes in mid-latitudes of the western and eastern North Pacific during 1999-2006: Recent results utilizing voluntary observation ships. *J. Meteor. Soc. Japan,* **88,** 883–898, doi:10.2151/jmsj.2010-602.

Telszewski, M., and Coauthors, 2009: Estimating the monthly pCO_2 distribution in the North Atlantic using a self-organizing neural network. *Biogeosciences,* **6,** 1405–1421, doi:10.5194/bg-6-1405-2009.

Wanninkhof, R., 1992: Relationship between wind-speed and gas-exchange over the ocean. *J. Geophys. Res.,* **97,** 7373–7382, doi:10.1029/92JC00188.

——, and Coauthors, 2013: Global ocean carbon uptake: Magnitude, variability and trends. *Biogeosciences,* **10,** 1983–2000, doi:10.5194/bg-10-1983-2013.

Weiss, R. F., 1974: Carbon dioxide in water and seawater: The solubility of a non-ideal gas. *Mar. Chem.,* **2,** 203–215, doi:10.1016/0304-4203(74)90015-2.

Wilamowski, B. M., and H. Yu, 2010: Improved computation for Levenberg–Marquardt training. *IEEE Trans. Neural Network,* **21,** 930–937, doi:10.1109/TNN.2010.2045657.

Wong, C. S., F. A. Whitney, D. W. Crawford, K. Iseki, R. J. Matear, W. K. Johnson, and J. S. Page, 1999: Seasonal and interannual variability in particle fluxes of carbon, nitrogen and silicon from time series of sediment traps at Ocean Station P, 1982–1993: Relationship to changes in subarctic primary productivity. *Deep-Sea Res. II,* **46,** 2735–2760, doi:10.1016/S0967-0645(99)00082-X.

——, J. R. Christian, S.-K. E. Wong, J. Page, L. Xie, and S. Johannessen, 2010: Carbon dioxide in surface seawater of the eastern North Pacific Ocean (Line P), 1973–2005. *Deep-Sea Res. I,* **57,** 687–695, doi:10.1016/j.dsr.2010.02.003.

Zeng, J. Y., Y. Nojiri, P. P. Murphy, C. S. Wong, and Y. Fujinuma, 2002: A comparison of $\triangle pCO_2$ distributions in the northern North Pacific using results from a commercial vessel in 1995–1999. *Deep-Sea Res. II,* **49,** 5303–5315, doi:10.1016/S0967-0645(02)00192-3.